PHYSICAL REVIEW B **104**, 165403 (2021)

Orbital magnetoelectric effect in zigzag nanoribbons of *p*-band systems

Tarik P. Cysne,[1,*] Filipe S. M. Guimarães,[2] Luis M. Canonico,[3] Tatiana G. Rappoport,[4,5] and R. B. Muniz[1]
[1]*Instituto de Física, Universidade Federal Fluminense, 24210-346 Niterói, Rio de Janeiro, Brazil*
[2]*Jülich Supercomputing Centre, Forschungszentrum Jülich and JARA, 52425 Jülich, Germany*
[3]*Catalan Institute of Nanoscience and Nanotechnology, CSIC and BIST, Campus UAB, Bellaterra, 08193 Barcelona, Spain*
[4]*Instituto de Telecomunicações, Instituto Superior Tecnico, University of Lisbon, Avenida Rovisco Pais 1, 1049001 Lisbon, Portugal*
[5]*Instituto de Física, Universidade Federal do Rio de Janeiro, Caixa Postale 68528, 21941-972 Rio de Janeiro, Rio de Janeiro, Brazil*

(Received 25 February 2021; accepted 20 September 2021; published 1 October 2021)

Profiles of the spin and orbital angular momentum accumulations induced by a longitudinally applied electric field are explored in nanoribbons of *p*-band systems with a honeycomb lattice. We show that nanoribbons with zigzag borders can exhibit orbital magnetoelectric effects. More specifically, we have found that purely orbital magnetization oriented perpendicularly to the ribbon may be induced in these systems by means of the external electric field when sublattice symmetry is broken. The effect is rather general and may occur in other multiorbital materials.

DOI: 10.1103/PhysRevB.104.165403

I. INTRODUCTION

The magnetoelectric effect (MEE) observed in certain materials evinces the interrelationship between their magnetic and electrical properties. It consists of either the appearance of a magnetization induced by an applied electric field or the advent of electric polarization brought about by an external magnetic field. In the literature distinct names have been given to the MEE in order to highlight the main mechanisms involved and the relevant features of the systems where it manifests, but here, we shall generically refer to it simply as the magnetoelectric effect, without detriment to system specificities. [1–4].

The possibilities of utilizing electric field to control the magnetization (or the reverse) are certainly of great interest for device applications [5–9]. The MEE has been explored in various materials, including antiferromagnetic systems [10,11], multiferroic composites [12,13], and topological insulators [14–16], among others. From a microscopic point of view, contributions to the MEE may originate from the electronic spin and/or from its orbital angular momentum (OAM) [4]. In the second case, the phenomenon is often called the orbital magnetoelectric effect (OME) [17], which has also been investigated previously, for example, in helical lattices [18–20], graphene twisted bilayers [21], and magnetic nanoparticles [22].

An external electric field may also induce the appearance of an OAM current flowing transversely to the applied field direction. This is the so-called orbital Hall effect (OHE), which is similar to the spin Hall effect (SHE) [23] but, in contrast to the latter, does not necessarily require the presence of spin-orbit interaction to occur. Some years ago, the OHE was predicted to happen in semiconductors [24] and in metals, in which it can be very strong [25–27]. More recently, significant interest in the OHE and other orbital phenomena has been revived [28–36], especially in two-dimensional (2D) systems [37–49], with the aim of exploring novel possibilities for utilizing OAM currents to transmit and store information on nanoscopic scales [31,37].

The spin and orbital Hall effects may lead to angular momentum accumulations at the system's boundaries. In topological insulators, these borders host conducting electronic states that are topologically protected by symmetry and thus are robust to inhomogeneities. Nanoribbons of these materials exhibit these edge states and are quite useful for investigating their features. Recently, we examined the transport properties of charge, spin, and OAM in (p_x-p_y)-orbital systems with a 2D honeycomb lattice [43,44]. This model was introduced and intensively explored in the context of optical lattices, where it is possible to filter the p_z orbital by application of laser beams polarized in the z direction, leaving only the p_x and p_y orbitals effectively active [50–57]. More recently, it was found that this relatively simple model also describes fairly well the low-energy electronic properties of group-V-based 2D materials grown atop a SiC substrate. Here, the p_z-orbital filtering occurs naturally due to the interaction between the overlayer and the SiC substrate [58–62]. Despite its simplicity, the p_x-p_y tight-binding model on a honeycomb lattice exhibits a rich topological phase diagram as a function of the spin-orbit coupling and the sublattice asymmetry potential strengths [63]. We analyzed some of these phases and, under certain circumstances, found sizable OHE, with values that exceed those obtained for the SHE [44].

Quantum confinement effects caused by the nanoribbons' finite width may significantly alter the electronic states and transport properties of a system [64–67]. Quite generally, they depend upon the ribbon's breadths and edge shapes, enabling the emergence of novel attributes and functionalities [68–70]. Hence, it is instructive to inquire how nanoribbons of these (p_x-p_y)-orbital materials respond to an electric field applied along the stripe axis and, in particular, evaluate the spin and OAM disturbances induced by it.

---

[*] tarik.cysne@gmail.com

Here, we calculate profiles of the spin and OAM accumulations produced by a longitudinally applied electric field on nanoribbons of p-band systems. We show that a MEE can take place in zigzag (ZZ) nanoribbons of these materials in which a purely orbital magnetization is brought about by this external field. The possibility of controlling the appearance of orbital magnetization by means of an electric field increases the prospects of using these systems for orbitronic applications.

II. MODEL AND METHODS

We consider a tight-binding model with two atomic orbitals (p_x, p_y) per site on a honeycomb lattice [58,63], described by the Hamiltonian

$$\mathcal{H} = \sum_{\langle ij\rangle}\sum_{\mu\nu s}\left(t_{ij}^{\mu\nu} + \epsilon_i\delta_{ij}\delta_{\mu\nu}\right)p^{\dagger}_{i\mu s}p_{j\nu s} + \lambda_I\sum_{i\mu\nu s} s^z_{ss}L^z_{\mu,\nu}p^{\dagger}_{i\mu s}p_{i\nu s}, \tag{1}$$

where the first line represents the electronic kinetic energy plus a spin-independent local potential and the second one describes the intrinsic atomic spin-orbit interaction in the subspace spanned by the p_x-p_y orbitals. Here, i and j denote the honeycomb lattice sites positioned at $\vec{R}_i$ and $\vec{R}_j$, respectively. The symbol $\langle ij\rangle$ indicates that the sum runs over only nearest-neighbor atoms. The operator $p^{\dagger}_{i\mu s}$ creates an electron of spin $s = \uparrow, \downarrow$ in the atomic orbitals p_μ ($\mu = x, y$) located at $\vec{R}_i$. ϵ_i represents the on-site atomic energy plus a staggered local potential V_i that breaks the inversion symmetry between the two interpenetrating triangular sublattices A and B; $V_i = +V_{\rm AB}$ ($-V_{\rm AB}$) when i belongs to sublattice A (B). The hopping integrals $t_{ij}^{\mu\nu}$ between orbitals $p_{i\mu}$ and $p_{j\nu}$ are parametrized according to the standard Slater-Koster tight-binding formalism [71] and may be expressed in terms of the usual two-center integrals, $V_{pp\sigma}$ and $V_{pp\pi}$. λ_I represents the strength of the intrinsic spin-orbit coupling (SOC), s^z_{ss} are the diagonal elements of the usual Pauli matrix diag$(1, -1)$, and $L^z_{\mu,\nu}$ are matrix elements of the OAM operator represented in $p_{x,y}$ subspace. More details on the Hamiltonian can be found in the Appendix.

In our calculations, the energy origin is chosen to coincide with the energy level of the atomic orbitals $p_{x,y}$. For simplicity, we assume that $V_{pp\pi} = 0$ and take $V_{pp\sigma} = 1$ as our energy unit. We shall explore the accumulations of spin and OAM induced by an electric field applied along the nanoribbon axis direction. Figure 1(a) illustrates a nanoribbon with ZZ edges in which the atoms belonging to sublattices A and B are represented by white and black circles, respectively. It is finite along the transverse $\hat{y}$ direction and, in general, is N atomic lines wide, which are identified by integer numbers $\ell = 1, \ldots, N$, as schematically illustrated in Fig. 1(a) for $N = 5$. Figures 1(b) to 1(e) show the calculated band energy spectra for ZZ nanoribbons with 15 lines in breadth for different values of $V_{\rm AB}$ and λ_I. Figures 1(b) and 1(c) display results for nanoribbons taken from 2D bulk systems in which the central energy band gap ΔE_0 is nontopological. This is confirmed by the absence of edge states crossing this energy range, where the system is an ordinary insulator. For $\lambda_I = 0.10$ and $V_{\rm AB} = 0.15$, depicted in Fig. 1(c), the bulk system is in the A1 phase, which is categorized by the set of $\uparrow$-spin band Chern numbers $\mathcal{C}^{\rm A1}_s = (1, -1, 1, -1)$ in Ref. [63]. In this case, the system exhibits two lateral energy band gaps ($\Delta E_{\bar{1}}$ and ΔE_1) that are topological, in addition to the nontopological one ΔE_0. Figure 1(c) shows that $\Delta E_{\bar{1}}$ and ΔE_1 are crossed by chiral edge states in the ribbon geometry, as expected [72].

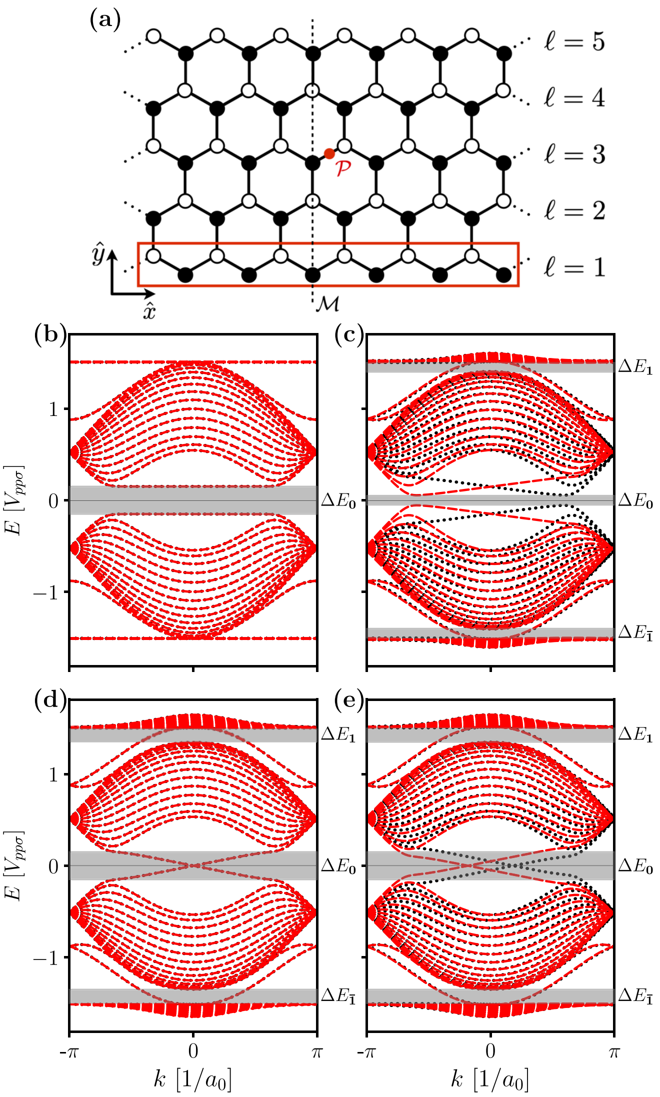

FIG. 1. (a) Schematic representation of a ZZ nanoribbon comprising five atomic lines that are identified by integers numbers $\ell = 1, \ldots, 5$; the atoms in sublattice A (B) are depicted by white (black) circles. The vertical dashed black line indicates the plane of mirror symmetry $\mathcal{M}$, which contains an AB-site vertical bond in the ZZ nanoribbon. The red circle indicates the spatial-inversion symmetry center $\mathcal{P}$ of the ZZ nanoribbon in the absence of the sublattice potential. (b)–(e) The calculated electronic energy bands for a ZZ nanoribbon with 15 lines wide. The wave vector k is written in units of a_0^{-1}, where a_0 represents the lattice constant. Black dotted and red dashed lines refer to $\uparrow$- and $\downarrow$-spin bands, respectively. Results calculated for $V_{\rm AB} = 0.15$ with (b) $\lambda_I = 0$ and (c) 0.10. (d) The results calculated with $\lambda_I = 0.15$ and $V_{\rm AB} = 0$ and (e) the results obtained with $\lambda_I = 0.15$ and $V_{\rm AB} = 0.05$. The gray stripes highlight the 2D bulk energy band gaps denoted by $\Delta E_{\bar{1}}$, ΔE_0, and ΔE_1.

Figures 1(d) and 1(e) display the energy bands for nanoribbons extracted from 2D systems in the B1 phase, classified by $\mathcal{C}_s^{\rm B1} = (1, 0, 0, -1)$, where they exhibit three topologically nontrivial bulk energy band gaps, within which the systems behave as a quantum spin Hall insulator [44,63]. We clearly see in Figs. 1(d) and 1(e) that all three gaps are crossed by edge states. As depicted in Fig. 1(b) and expected from our noninteracting-particle approach, the energy band spectrum for $\lambda_I = 0$ is spin degenerated. The same happens in the absence of $V_{\rm AB}$, as exemplified in Fig. 1(d). This is due to a combination of time-reversal symmetry and spatial inversion. However, when the sublattice symmetry is broken, SOC lifts this degeneracy, giving rise to spin-split energy bands, as illustrated in Figs. 1(c) and 1(e).

We calculate the spin $\delta\langle\hat{S}_\ell^z\rangle$ and OAM $\delta\langle\hat{L}_\ell^z\rangle$ accumulations per atom induced at each atomic line ℓ in the nanoribbons by an applied electric field. For this purpose, we utilize linear response theory following the same procedure described in Refs. [29,30]. The electric field is applied in plane, along the longitudinal $\hat{x}$ direction, as depicted in Fig. 1(a). Up to linear order in the perturbing field, the interband and intraband contributions to the change in the expectation value of an observable $\delta\langle\hat{O}_\ell\rangle$ due to the applied field are given by

$$\delta\langle\hat{O}_\ell\rangle^{\rm Intra} = -\frac{e\hbar\mathcal{E}_x}{2\Gamma}\sum_{n,k}\frac{\partial f_{nk}}{\partial E} \times \langle nk|\hat{O}_\ell|nk\rangle\langle nk|v(k)|nk\rangle, \qquad (2a)$$

$$\delta\langle\hat{O}_\ell\rangle^{\rm Inter} = e\hbar\mathcal{E}_x\sum_{n,m,k}(f_{nk}-f_{mk}) \times {\rm Im}\left[\frac{\langle nk|\hat{O}_\ell|mk\rangle\langle mk|v(k)|nk\rangle}{(E_{nk}-E_{mk}+i\eta)^2}\right]. \qquad (2b)$$

Here, $\hat{O}_\ell$ may represent either the spin $\hat{S}_\ell^z$ or the OAM $\hat{L}_\ell^z$ operators projected on line ℓ [73]. For the OAM operator, we follow Ref. [30] and use the intra-atomic orbital approximation. E_{nk} are the eigenvalues, and $|nk\rangle$ are the corresponding eigenvectors of the Hamiltonian given by Eq. (1) evaluated in the reciprocal space; n denotes the energy band index, k is the wave vector, and f_{nk} symbolizes the Fermi-Dirac distribution function associated with the state $|nk\rangle$. $\hat{v}(k) = \hbar^{-1}(\partial\hat{H}(k)/\partial k)$ is the velocity operator, e is the modulus of the electronic charge, and $\mathcal{E}_x$ denotes the intensity of the applied electric field. $\Gamma = \hbar/(2\tau)$, where τ is the momentum relaxation time, is treated here as a phenomenological parameter that simulates effects of disorder in the transport properties of the nanoribbons within the constant relaxation-time approximation [30,74]; η is a small positive quantity arising from a conventional artifice to ensure that the external perturbation is turned on adiabatically.

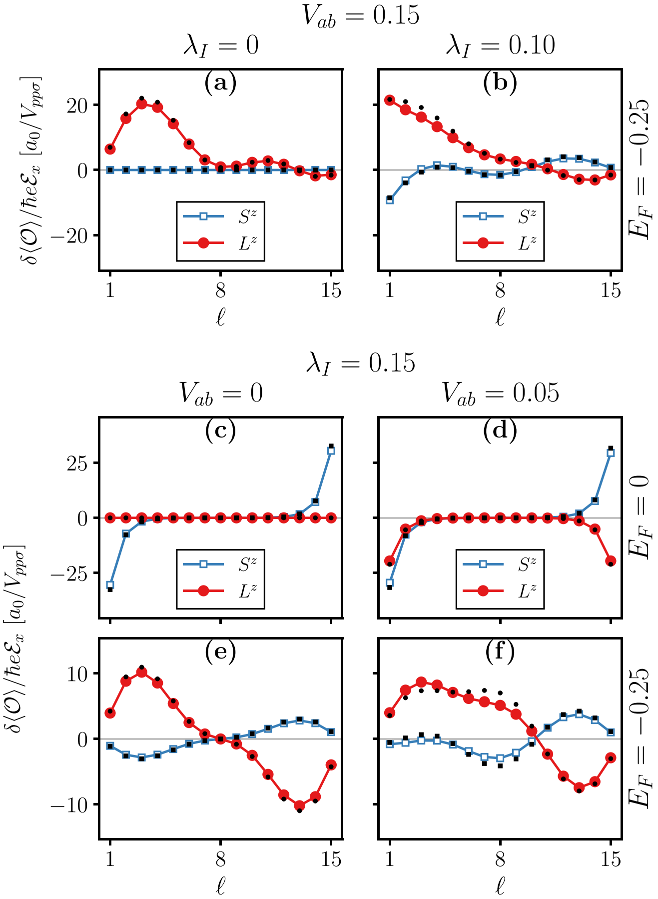

FIG. 2. Spin and OAM accumulation profiles induced by an applied electric field across ZZ nanoribbons with 15 atomic lines wide. $\delta\langle S_\ell^z\rangle$ and $\delta\langle L_\ell^z\rangle$ are calculated per atom in each atomic line ℓ of the ribbon. Results for $V_{\rm AB} = 0.15$ and $E_F = -0.25$ with (a) $\lambda_I = 0$ and (b) 0.10. Results obtained for $V_{\rm AB} = 0$ and $\lambda_I = 0.15$ with (c) $E_F = 0$ and (e) $E_F = -0.25$. (d) and (f) Results for $V_{\rm AB} = 0.05$, $\lambda_I = 0.15$, and the same values of E_F as in (c) and (e), respectively. Black squares and circles represent the results obtained by means of an alternative approach (see text) for the spin and OAM accumulations, respectively. Here, we used $\Gamma = 10^{-3}$.

III. RESULTS AND DISCUSSION

We consider a ZZ nanoribbon with 15 atomic lines and calculate the spin and OAM accumulations per atom induced by the applied electric field in each one of these lines. We start with the two cases in which the central energy band gap ΔE_0 of the 2D system is nontopological, namely, when $V_{\rm AB} = 0.15$ with $\lambda_I = 0$ and 0.10, whose energy bands are displayed in Figs. 1(b) and 1(c), respectively. In these circumstances, both the induced spin and OAM accumulations vanish for $E_F = 0$, which is compatible with the fact that the bulk 2D system for those sets of parameters is an ordinary insulator that shows neither SHE nor OHE at this Fermi energy (see Ref. [44]). However, beyond the energy gap ΔE_0 (e.g., for $E_F = -0.25$), the OAM accumulation is not zero, as Figs. 2(a) and 2(b) illustrate. Figure 2(a) reveals that outside the range of ΔE_0 we obtain OAM accumulation throughout the ribbon, even in the absence of SOC. While the induced spin accumulation in this case vanishes (as expected), the OAM profile is finite. Its most striking feature is the lack of symmetry with respect to the ribbon axis, which is markedly different from what one would expect solely from the OHE. Moreover, $\delta\langle L_t^z\rangle = \sum_\ell \delta\langle L_\ell^z\rangle \neq 0$, indicating the appearance of an induced net orbital magnetization—typical of an orbital magnetoelectric effect. Generally, the magnetization originates from spin and orbital magnetic moments, but in this specific case there is no spin contribution, and the induced magnetization has solely orbital character. Figure 2(b) shows that, for a nanoribbon extracted from a 2D system in the A1 phase, both the induced spin and OAM accumulation profiles are finite in the metallic regime and also *asymmetric* with respect to the ribbon axis. By summing the contributions of all lines, we find that the net magnetization remains purely orbital, as the total spin contribution vanishes. We shall now explore some cases in which the nanoribbons are extracted from 2D systems in the B1 phase, where all three energy band gaps are topological, as illustrated in Figs. 1(d) and 1(e). For $\lambda_I = 0.15$ and in the absence of V_{AB}, we see in Fig. 2(c) that sizable spin accumulations with opposite signs appear near the nanoribbon's edges for $E_F = 0$, whereas $\delta\langle L^z_\ell\rangle = 0\ \forall\ \ell$. This is what one would expect from the SHE and is also consistent with the fact that in the B1 phase the 2D system behaves as a quantum spin Hall insulator that displays no orbital Hall effect within ΔE_0 [44]. In contrast, by moving the Fermi level outside of ΔE_0 to $E_F = -0.25$, we observe in Fig. 2(e) that the induced OAM is finite. Here, both the induced spin and OAM accumulations are much more spread across the ribbon and not so restricted to the borders as in the case of $E_F = 0$. Nevertheless, they are both *antisymmetric* with respect to the ZZ ribbon axis and hence do not lead to a net magnetization, as the spin and orbital Hall effects forecast [44]. Moreover, when the sublattice symmetry is broken by a staggered potential $V_{\mathrm{AB}} = 0.05$, different profiles emerge. For example, in Fig. 2(d), we obtain an induced spin accumulation profile for $E_F = 0$ that is rather similar to the previous case, having antisymmetric character with respect to the nanoribbon axis, as one would expect from the SHE. However, the induced OAM profile across the ribbon is *symmetric* with respect to the nanoribbon axis, which is not expected from the OHE and clearly leads to a nonzero net orbital magnetization when we sum over all lines. In Fig. 2(f), asymmetric profiles for both the induced spin and OAM accumulations are also revealed for $E_F = -0.25$. Here, by summing over all lines the spin contribution once again vanishes, and the resulting induced magnetization acquires a purely orbital character.

In order to confirm our predictions, we repeated our calculations employing an alternate approach, described in Refs. [75,76]. It considers a spatially uniform and time-dependent harmonic electric field with small amplitude $\mathcal{E}_x$ that within linear response theory gives rise to a local spin and OAM disturbances per atom in line ℓ given by

$$\delta\langle \mathcal{O}_\ell(t)\rangle = -\lim_{\omega\to 0}\frac{e\mathcal{E}_x}{\hbar\omega}\,\mathrm{Im}\{e^{-i\omega t}\mathcal{D}_\ell(\omega)\}, \tag{3}$$

where

$$\mathcal{D}_\ell(\omega) = \sum_{\substack{k\\ s_1s_2s_3}}\ \sum_{\substack{\ell_1\ell_2\\ \mu\nu\gamma\xi}} \mathcal{O}^{s_1s_2}_{\mu\nu}\,\chi^{s_1s_2s_3s_3\mu\nu\gamma\xi}_{\ell\ell\ell_1\ell_2}(k,\omega)\,\frac{\partial t^{\gamma\xi}_{\ell_2\ell_1}(k)}{\partial k}. \tag{4}$$

Here, s_1, s_2, and s_3 designate the ↑ and ↓ spin directions; μ, ν, γ, and ξ denote the p_x and p_y atomic orbitals; and ℓ, ℓ_1, and ℓ_2 label the atomic lines. The matrix elements $\mathcal{O}^{s_1s_2}_{\mu\nu} = S^z_{s_1s_2}\delta_{\mu\nu}$ for the spin accumulation, $\mathcal{O}^{s_1s_2}_{\mu\nu} = L^z_{\mu\nu}\delta_{s_1s_2}$ for the OAM disturbance. In our case, since we are neglecting the electronic Coulomb interaction, $\chi(k,\omega)$ represent generalized noninteracting spin susceptibilities. The results obtained with this method for the induced spin and OAM accumulations are depicted in Fig. 2 by black squares and circles, respectively. The agreement between the two approaches is excellent and corroborates our findings.

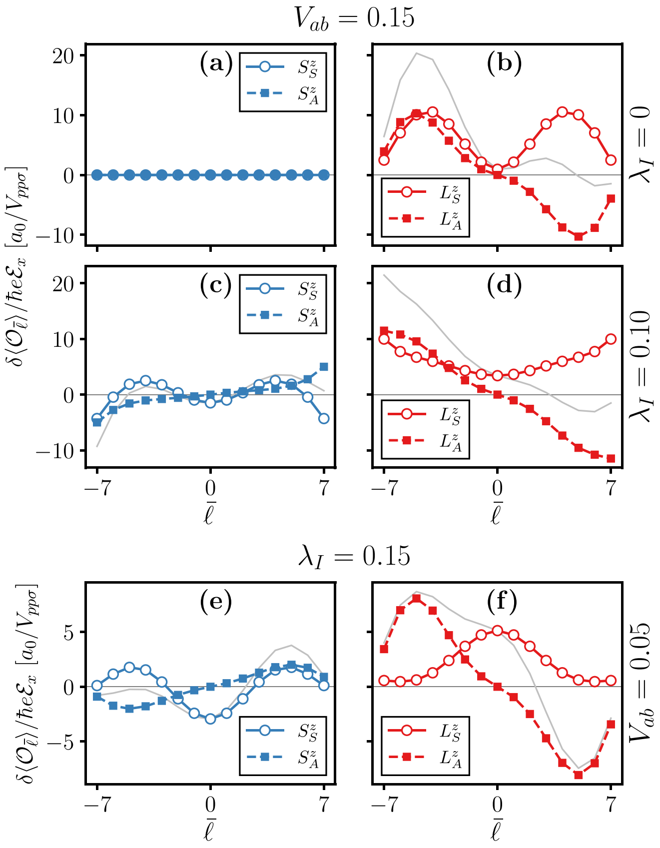

FIG. 3. Decomposition into symmetric and antisymmetric components of the induced spin and OAM profiles depicted in Figs. 2(a), 2(b), and 2(f). The original profiles are reproduced here by the gray lines. (a) and (b) The decomposition of the spin and OAM profiles depicted in Fig. 2(a), calculated for $V_{\mathrm{AB}} = 0.15$, $\lambda_I = 0$, and $E_F = -0.25$. (c) and (d) The decomposition of the spin and OAM profiles depicted in Fig. 2(b), calculated for $V_{\mathrm{AB}} = 0.15$, $\lambda_I = 0.10$, and $E_F = -0.25$. (e) and (f) The decomposition of the spin and OAM profiles depicted in Fig. 2(f), calculated for $V_{\mathrm{AB}} = 0.05$, $\lambda_I = 0.15$, and $E_F = -0.25$.

To extract some physical insights into the different effects that contribute to the spin and OAM responses on the ZZ nanoribbon, we further explore the cases with asymmetric profiles exhibited in Figs. 2(a), 2(b), and 2(f). It is instructive to identify their symmetric and antisymmetric components. To this end it is useful to relabel the atomic lines by $\bar\ell \in [-7, 7]$. The antisymmetric ($-$) and symmetric ($+$) contributions to the profiles are obtained with $\delta\langle\hat{\mathcal{O}}_{\bar\ell}\rangle^{\mp} = (\delta\langle\hat{\mathcal{O}}_{\bar\ell}\rangle \mp \delta\langle\hat{\mathcal{O}}_{-\bar\ell}\rangle)/2$ and are shown in Fig. 3. We identify the antisymmetric contributions to the induced spin ($\langle\delta S^z\rangle_A$) and OAM ($\langle\delta L^z\rangle_A$) profiles as arising from the spin and orbital Hall effects [44], respectively, and the symmetric ones ($\langle\delta S^z\rangle_S$ and $\langle\delta L^z\rangle_S$) are ascribed to the MEE. Clearly, a nonzero induced magnetization can come from only the symmetric components. However, the appearance of a symmetric contribution does

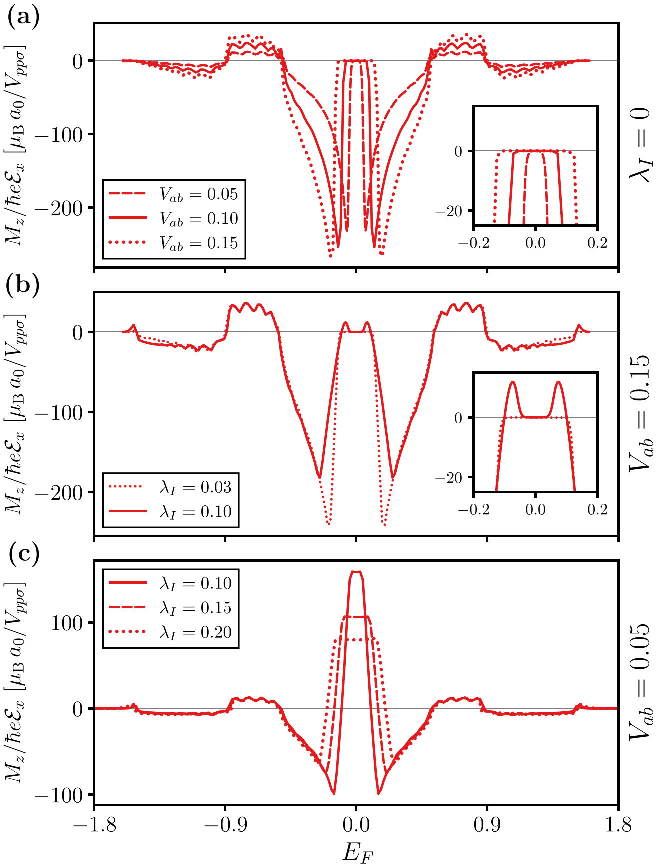

FIG. 4. Electric field induced orbital magnetization M_z per unit cell calculated as a function of E_F for a ZZ nanoribbon with 15 lines. (a) Results obtained for $\lambda_I = 0$ and three distinct values of $V_{\rm AB}$. The inset highlights the calculated values of $M_z(E_F)$ around $E_F = 0$. (b) Results for nanoribbons taken from a 2D system in the A1 phase, calculated for $V_{\rm AB} = 0.15$ with $\lambda_I = 0.03$ and 0.10. (c) Results calculated for nanoribbons taken from a 2D system in the B1 phase with $V_{AB} = 0.05$ for three different values of λ_I.

not necessarily lead to a nonzero magnetization. For example, the symmetric spin contribution to the total induced magnetization illustrated in Figs. 3(c) and 3(e) is zero, i.e., $\sum_{\ell=-7}^{7} \langle \delta S_\ell^z \rangle_S = 0$. In contrast, the symmetric orbital components depicted in Figs. 3(b), 3(d), and 3(f) clearly lead to a nonzero magnetization that is purely orbital, characterizing an orbital magnetoelectric effect.

We shall now examine how the total induced orbital magnetization per unit cell of the ZZ nanoribbon ($M_z = -\mu_{\rm B}\langle \delta L_t^z \rangle$) is influenced by the sublattice symmetry-breaking potential $V_{\rm AB}$, the SOC strength λ_I, and the Fermi energy E_F. Here, $\mu_{\rm B}$ denotes the Bohr magneton. We start with the case in which $\lambda_I = 0$, where ΔE_0 is nontopological and is not crossed by conducting edge states in the ribbon geometry. Figure 4(a) shows results for M_z calculated as a function of energy for different values of $V_{\rm AB}$. The energy band gaps increase with $V_{\rm AB}$, and within them the OME vanishes. However, outside and close to the energy gap borders, the OME assumes quite large values even in the absence of SOC, indicating that with the use of a gate voltage one may control the advent of the OME in this case. In Fig. 4(b), we show results calculated for $V_{\rm AB} = 0.15$ and $\lambda_I = 0.03$ and 0.10, which represent nanoribbons extracted from a 2D system in the A1 phase. Here, we see once more that for energies within the corresponding central energy band gaps, where the system is an ordinary insulator, there is also no OME. Nevertheless, in the metallic regime, the OME may reach relatively high values that increase as the SOC diminishes. Finally, in Fig. 4(c) we display results calculated for $V_{\rm AB} = 0.05$ and three different values of λ_I. They all refer to nanoribbons extracted from a 2D system in the B1 phase, where, in contrast to the two previous cases, the central energy band gap is topological and crossed by conducting edge states in the stripe geometry, as shown in Figs. 1(d) and 1(e). We clearly see that the OME is finite and relatively large within ΔE_0, changing sign when E_F crosses its borders and also attaining fairly high values outside the range of ΔE_0. Once again, we note that in this phase, which requires $\lambda_I > V_{\rm AB}$, the maximum intensity of the OME also reduces as the SOC increases. Here, it seems also possible to manipulate the direction of the induced orbital magnetization with the of use of gate voltages.

It is noteworthy that the appearance of the orbital magnetoelectric effect in these nanoribbons requires sublattice symmetry breaking. Spin-orbit coupling influences the OME but is not a necessary ingredient for its occurrence. Our results reveal that with the increase of the SOC strength the maximum intensity of the OME actually reduces. They also show that the OME vanishes in the absence of conducting states at the Fermi energy, which typifies a current-induced magnetization effect, also called the kinetic magnetoelectric effect [2,3]. This is consistent with the fact that the induced orbital magnetization is totally dominated by the intraband contribution [Eq. (2a)] for the cases we have examined. Up to first order in the applied field, the magnetoelectric effect is well described by the magnetoelectric susceptibility tensor $\hat{\alpha}$, which links the components of the induced magnetization to the applied electric field: $M_i = \sum_j \alpha_{ij}\mathcal{E}_j$, where i and j here denote the Cartesian directions x, y, z and α_{ij} represent the matrix elements of $\hat{\alpha}$. The general form of $\hat{\alpha}$ may be determined by symmetry arguments [77]. Parity and time-reversal symmetries in particular play an important role in the magnetoelectric effect. For example, it is possible to show that the intraband contribution to M_z requires inversion symmetry to be broken, as pointed out in Refs. [78,79]. However, to activate the interband contribution [Eq. (2b)] it is also necessary to break time-reversal symmetry. This justifies the absence of interband contributions in our calculations since our Hamiltonian breaks spatial inversion symmetry in the presence of $V_{\rm AB}$ but remains invariant with time reversal. It is also worth mentioning that the crystal structure of the 2D bulk system in the presence of $V_{\rm AB}$ belongs to point group D_{3h}, which leads to $\alpha_{zx} = 0$ [80] and hence does not allow the OME to take place. Nevertheless, for the zigzag nanoribbon with sublattice asymmetry, the point group is reduced to C_{2v}, with the principal axis lying in plane along the $\hat{y}$ direction, which allows nonzero values of α_{zx} [81].

In Figs. 4(a) and 4(b) we see that the maximum calculated value for the total induced orbital magnetization per unit cell of the ZZ nanoribbon $M_z/(\hbar e\mathcal{E}_x)$ is approximately $200\mu_{\rm B}a_0/V_{pp\sigma}$ in the metallic regime close to the energy band gap borders. Thus, for $a_0/V_{pp\sigma} \approx 0.25$ nm/eV (typical of the group-V elements/SiC) and for $\mathcal{E}_x = 1 \times 10^5$ V/m, we obtain a value of $M_z \approx 5 \times 10^{-3}\mu_B$. This is more than one order of magnitude larger than the current-induced magnetic moment for Au(111) and is slightly larger than the results obtained for Bi/Ag(111) and for the α-Sn(001) surface [82]. The results depicted in Fig. 4(c) show that the absolute value of M_z for energies within the bulk topological energy band gap ΔE_0 is a little bit smaller than but still comparable to that in the previous case for the same value of $\Gamma = 10^{-3}$, which corresponds to a momentum relaxation time $\tau \approx 0.17$ ps. In this case, it is worth noting that the appearance of the induced magnetization is mediated by conducting edge states that are topologically protected against disordered scattering. Therefore, the induced magnetization may be much larger since it increases linearly with τ, according to Eq. (2a).

Here, since the OME is mediated by only conducting states, it may be useful to associate the induced magnetization with the components of the electric-current density $\mathcal{J}_i$ as $M_i = \sum_j \beta_{ij}\mathcal{J}_j$ [18]. In our case $M_z = \beta_{zx}\mathcal{J}_x$, where $\beta_{zx} = \alpha_{zx}\rho_{xx}$, with ρ_{xx} representing the longitudinal resistivity. Since $\alpha_{zx} \propto \tau$ and $\rho_{xx} \propto 1/\tau$, β_{zx} does not depend upon τ. It is also noteworthy that the staggered local potential ($V_i = \pm V_{AB}$) creates electric dipoles that cancel out in the bulk but not for nanoribbons with zigzag edges, where a net in-plane polarization P_y emerges along the $\hat{y}$ direction, leading to a polar system with no inversion symmetry. In this case, the induced orbital magnetization $\vec{M} \propto \vec{P} \times \vec{\mathcal{J}}$, which results in nonzero values of $M_z \propto P_y\mathcal{J}_x$. For nanoribbons with armchair borders, however, P_y vanishes, and so does the induced orbital magnetization, as our calculations confirm.

IV. CONCLUSIONS

In summary, we have shown that nanoribbons with zigzag borders of p_x-p_y band systems in a honeycomb lattice can exhibit fairly large orbital magnetization induced by an electric current flowing along the ribbon axis when sublattice symmetry is broken. We have explored nanoribbons extracted from 2D systems in two distinct phases. In the first one, the 2D system is an ordinary insulator at the neutrality point, and the ribbon exhibits no induced magnetization for Fermi energies within the energy band gap. Nevertheless, it shows significant values of OME outside this energy range, even in the absence of spin-orbit coupling. In the second case, the 2D system is a topological insulator that has conducting edge states crossing the energy band gap in the nanoribbon geometry. In this situation, the induced orbital magnetization is fairly large for energies within the 2D bulk gap and also attains high values with opposite sign just beyond the gap boundaries. In both cases, the induced orbital magnetization is oriented perpendicularly to the nanoribbon plane. Our results indicate that it may be controlled by a gate voltage, a basic requirement for device applications.

ACKNOWLEDGMENTS

We acknowledge CNPq (Brazil), CAPES (Brazil), FAPERJ (Brazil), and INCT Nanocarbono for financial support. T.G.R. acknowledges funding from Fundação para a Ciência e a Tecnologia and Instituto de Telecomunicações, Grant No. UID/50008/2020 in the framework of the project Sym-Break. T.G.R. thankfully acknowledges the computer resources at MareNostrum and the technical support provided by Barcelona Supercomputing Center (FI-2020-2-0033). L.M.C. acknowledges funding from The Army Research Office under Grant No. W911NF-21-1-0004. ICN2 is funded by the CERCA Programme/Generalitat de Catalunya and supported by the Severo Ochoa Centres of Excellence program, funded by the Spanish Research Agency (Grant No. SEV-2017-0706). F.S.M.G. gratefully acknowledge the computing time granted through JARA on the supercomputer JURECA [83] at Forschungszentrum Jülich. Helpful conversations with Prof. P. Venezuela are gratefully acknowledged.

APPENDIX: TIGHT-BINDING MODEL FOR ZIGZAG NANORIBBON

In this Appendix, we present details of the p_x-p_y tight-binding model [Eq. (1)] used to compute the spin and OAM responses to an external electric field in ZZ nanoribbons.

1. Kinetic term

The hopping amplitudes between orbitals on different sites i and j are computed using the Slater-Koster method [71]. They are written in terms of the direction cosines connecting sites i and j, $n_\mu(i,j)$ ($\mu = x, y, z$), and of the two centers integrals, $V_{pp\sigma}$ and $V_{pp\pi}$,

$$t_{\mu,\mu}(i,j) = n_\mu^2(i,j)V_{pp\sigma} + \left[1 - n_\mu^2(i,j)\right]V_{pp\pi}, \tag{A1}$$

$$t_{\mu,\nu}(i,j) = -n_\mu(i,j)n_\nu(i,j)(V_{pp\pi} - V_{pp\sigma}). \tag{A2}$$

We restrict the hopping of our model to nearest-neighbor sites, which have vectors, on the coordinate system in Fig. 1(a), pointing along $\vec{e}_1 = (a_0/\sqrt{3})(0,1)$, $\vec{e}_2 = (a_0/\sqrt{3})(-\sqrt{3}/2, -1/2)$, and $\vec{e}_3 = (a_0/\sqrt{3})(\sqrt{3}/2, -1/2)$. Here, a_0 is the lattice constant. We now define the Slater-Koster matrix of hoppings connecting site i to its mth neighbor ($m = 1, 2, 3$) as

$$t_m(k) = \sum_{\mu,\nu=x,y} |p_\mu\rangle t_{\mu,\nu}(m)\exp(ik\,\vec{e}_m\cdot\hat{x})\langle p_\nu|, \tag{A3}$$

where $t_{\mu,\nu}(m)$ are given by Eqs. (A1) and (A2). In the unit cell of the ZZ nanoribbon, there are two inequivalent sites, one at sublattice A and the other at sublattice B. The Hilbert space of the ZZ nanoribbon is spanned by $\mathcal{H}^{zz} = \{|A,B\rangle \otimes |p_x, p_y\rangle \otimes |\ell\rangle\} \otimes |k\rangle$, where $|\ell\rangle$ is the quantum number associated with the line of the ribbon. The hopping integral $t_{2,3}$ occurs within the same line ℓ. We define the matrix of hoppings in the same line, in the basis $|A,B\rangle$, as

$$h_{l0}(k) = \begin{bmatrix} 0 & t_2(k) + t_3(k) \\ [t_2(k) + t_3(k)]^\dagger & 0 \end{bmatrix}. \tag{A4}$$

The matrices of hoppings that switch the lines are

$$h_{l+}(k) = \begin{bmatrix} 0 & t_1(k) \\ 0 & 0 \end{bmatrix}; \quad h_{l-}(k) = \begin{bmatrix} 0 & 0 \\ t_1^\dagger(k) & 0 \end{bmatrix}. \tag{A5}$$

Using these matrices, we built the kinetic term of the Hamiltonian in Eq. (1) in the reciprocal space for a ZZ nanoribbon,

$$H_{\text{kin}}(k) = \begin{bmatrix} h_{l0}(k) & h_{l-}(k) & 0 & \dots & 0 \\ h_{l+}(k) & h_{l0}(k) & h_{l-}(k) & \dots & 0 \\ 0 & h_{l+}(k) & h_{l0}(k) & \dots & 0 \\ \vdots & \vdots & \vdots & \ddots & \vdots \\ 0 & 0 & 0 & \dots & h_{l0}(k) \end{bmatrix}. \tag{A6}$$

For a ribbon with N lines, the matrix in Eq. (A6) has a tridiagonal block form with N diagonal blocks $h_{l0}(k)$.

2. SOC and sublattice potential

The component L^z of the orbital angular momentum operator at atomic approximation [30,84,85] in the basis $\{|p_x\rangle, |p_y\rangle\}$ is written as

$$L^z = \begin{bmatrix} 0 & -i \\ i & 0 \end{bmatrix}. \tag{A7}$$

The spin-orbit coupling term is written as

$$H_{\text{SOC}} = \lambda_I S^z L^z \mathbb{1}_\sigma \mathbb{1}_\ell, \tag{A8}$$

where $S^z = \text{diag}(1, -1)$ is the Pauli matrix related to electron spin and $\mathbb{1}_\sigma$ ($\mathbb{1}_\ell$) is the identity operator in the sublattice (line) degree of freedom. The sublattice potential term is defined as

$$H_{\text{AB}} = V_{\text{AB}} \mathbb{1}_S \mathbb{1}_L \sigma_z \mathbb{1}_\ell, \tag{A9}$$

where, now, $\sigma_z = \text{diag}(1, -1)$ is the Pauli matrix related to the sublattice degree of freedom and $\mathbb{1}_S$ ($\mathbb{1}_L$) is the identity operator in the spin (orbital) space.

[1] A. M. Essin, J. E. Moore, and D. Vanderbilt, Phys. Rev. Lett. **102**, 146805 (2009).

[2] S. S. Tsirkin, P. A. Puente, and I. Souza, Phys. Rev. B **97**, 035158 (2018).

[3] C. Şahin, J. Rou, J. Ma, and D. A. Pesin, Phys. Rev. B **97**, 205206 (2018).

[4] G. Massarelli, B. Wu, and A. Paramekanti, Phys. Rev. B **100**, 075136 (2019).

[5] S. Fusil, V. Garcia, A. Barthélémy, and M. Bibes, Annu. Rev. Mater. Res. **44**, 91 (2014).

[6] N. Ortega, A. Kumar, J. F. Scott, and R. S. Katiyar, J. Phys.: Condens. Matter **27**, 504002 (2015).

[7] Y. Cheng, B. Peng, Z. Hu, Z. Zhou, and M. Liu, Phys. Lett. A **382**, 3018 (2018).

[8] J.-M. Hu and C.-W. Nan, APL Mater. **7**, 080905 (2019).

[9] C. Xiao, Y. Ren, and B. Xiong, Phys. Rev. B **103**, 115432 (2021).

[10] Y. Yanagi, S. Hayami, and H. Kusunose, Phys. Rev. B **97**, 020404(R) (2018).

[11] P. Yanda, N. V. Ter-Oganessian, and A. Sundaresan, Phys. Rev. B **100**, 104417 (2019).

[12] Y. Lin, N. Cai, J. Zhai, G. Liu, and C.-W. Nan, Phys. Rev. B **72**, 012405 (2005).

[13] G. Bera, A. Surampalli, A. Mishra, P. Mal, V. R. Reddy, A. Banerjee, A. Sagdeo, P. Das, and G. R. Turpu, Phys. Rev. B **100**, 014436 (2019).

[14] V. Dziom, A. Shuvaev, A. Pimenov, G. V. Astakhov, C. Ames, K. Bendias, J. Böttcher, G. Tkachov, E. M. Hankiewicz, C. Brüne, H. Buhmann, and L. W. Molenkamp, Nat. Commun. **8**, 15197 (2017).

[15] H.-G. Zirnstein and B. Rosenow, Phys. Rev. B **96**, 201112(R) (2017).

[16] X.-L. Qi, T. L. Hughes, and S.-C. Zhang, Phys. Rev. B **78**, 195424 (2008).

[17] L. S. Levitov, Y. V. Nazarov, and G. M. Eliashberg, Sov. Phys. JETP **61**, 133 (1985).

[18] T. Yoda, T. Yokoyama, and S. Murakami, Nano Lett. **18**, 916 (2018).

[19] T. Yoda, T. Yokoyama, and S. Murakami, Sci. Rep. **5**, 12024 (2015).

[20] D. Hara, M. S. Bahramy, and S. Murakami, Phys. Rev. B **102**, 184404 (2020).

[21] W.-Y. He, D. Goldhaber-Gordon, and K. T. Law, Nat. Commun. **11**, 1650 (2020).

[22] P. Wang, E. Zhang, D. Toledo, I. T. Smith, B. Navarrete, N. Furman, A. F. Hernandez, M. Telusma, D. McDaniel, P. Liang, and S. Khizroev, Nano Lett. **20**, 5765 (2020).

[23] J. Sinova, S. O. Valenzuela, J. Wunderlich, C. H. Back, and T. Jungwirth, Rev. Mod. Phys. **87**, 1213 (2015).

[24] B. A. Bernevig, T. L. Hughes, and S.-C. Zhang, Phys. Rev. Lett. **95**, 066601 (2005).

[25] H. Kontani, T. Tanaka, D. S. Hirashima, K. Yamada, and J. Inoue, Phys. Rev. Lett. **100**, 096601 (2008).

[26] T. Tanaka, H. Kontani, M. Naito, T. Naito, D. S. Hirashima, K. Yamada, and J. Inoue, Phys. Rev. B **77**, 165117 (2008).

[27] H. Kontani, T. Tanaka, D. S. Hirashima, K. Yamada, and J. Inoue, Phys. Rev. Lett. **102**, 016601 (2009).

[28] S. Ding, A. Ross, D. Go, L. Baldrati, Z. Ren, F. Freimuth, S. Becker, F. Kammerbauer, J. Yang, G. Jakob, Y. Mokrousov, and M. Klaui, Phys. Rev. Lett. **125**, 177201 (2020).

[29] D. Go and H.-W. Lee, Phys. Rev. Research **2**, 013177 (2020).

[30] D. Go, F. Freimuth, J.-P. Hanke, F. Xue, O. Gomonay, K.-J. Lee, S. Blügel, P. M. Haney, H.-W. Lee, and Y. Mokrousov, Phys. Rev. Research **2**, 033401 (2020).

[31] J. Xiao, Y. Liu, and B. Yan, *Memorial Volume for Shoucheng Zhang* (World Scientific, 2021), Chap. 13, pp. 353–364.

[32] D. Go, D. Jo, C. Kim, and H.-W. Lee, Phys. Rev. Lett. **121**, 086602 (2018).

[33] S. Bhowal and S. Satpathy, Phys. Rev. B **102**, 201403(R) (2020).

[34] D. Jo, D. Go, and H.-W. Lee, Phys. Rev. B **98**, 214405 (2018).

[35] S. Beaulieu, J. Schusser, S. Dong, M. Schüler, T. Pincelli, M. Dendzik, J. Maklar, A. Neef, H. Ebert, K. Hricovini, M. Wolf, J. Braun, L. Rettig, J. Minar, and R. Ernstorfer, Phys. Rev. Lett. **125**, 216404 (2020).

[36] M. Schüler, T. Pincelli, S. Dong, T. P. Devereaux, M. Wolf, L. Rettig, R. Ernstorfer, and S. Beaulieu, arXiv:2103.17168.

[37] X. Mu, Y. Pan, and J. Zhou, npj Comput. Mater. **7**, 61 (2021).

[38] I. V. Tokatly, Phys. Rev. B **82**, 161404(R) (2010).

[39] F. Castro de Lima, G. J. Ferreira, and R. H. Miwa, Nano Lett. **19**, 6564 (2019).

[40] V. T. Phong, Z. Addison, S. Ahn, H. Min, R. Agarwal, and E. J. Mele, Phys. Rev. Lett. **123**, 236403 (2019).

[41] M. Ünzelmann, H. Bentmann, P. Eck, T. Kißlinger, B. Geldiyev, J. Rieger, S. Moser, R. C. Vidal, K. Kißner, L. Hammer, M. A. Schneider, T. Fauster, G. Sangiovanni, D. DiSante, and F. Reinert, Phys. Rev. Lett. **124**, 176401 (2020).

[42] J.-H. Park, C. H. Kim, J.-W. Rhim, and J. H. Han, Phys. Rev. B **85**, 195401 (2012).

[43] L. M. Canonico, T. G. Rappoport, and R. B. Muniz, Phys. Rev. Lett. **122**, 196601 (2019).

[44] L. M. Canonico, T. P. Cysne, T. G. Rappoport, and R. B. Muniz, Phys. Rev. B **101**, 075429 (2020).

[45] L. M. Canonico, T. P. Cysne, A. Molina-Sanchez, R. B. Muniz, and T. G. Rappoport, Phys. Rev. B **101**, 161409(R) (2020).

[46] S. Bhowal and S. Satpathy, Phys. Rev. B **102**, 035409 (2020).

[47] S. Bhowal and G. Vignale, Phys. Rev. B **103**, 195309 (2021).

[48] F. Xue, V. Amin, and P. M. Haney, Phys. Rev. B **102**, 161103(R) (2020).

[49] T. P. Cysne, M. Costa, L. M. Canonico, M. B. Nardelli, R. B. Muniz, and T. G. Rappoport, Phys. Rev. Lett. **126**, 056601 (2021).

[50] C. Wu and S. Das Sarma, Phys. Rev. B **77**, 235107 (2008).

[51] C. Wu, D. Bergman, L. Balents, and S. Das Sarma, Phys. Rev. Lett. **99**, 070401 (2007).

[52] C. Wu, Phys. Rev. Lett. **101**, 186807 (2008).

[53] C. Wu, Phys. Rev. Lett. **100**, 200406 (2008).

[54] S. Zhang, H.-H. Hung, and C. Wu, Phys. Rev. A **82**, 053618 (2010).

[55] W.-C. Lee, C. Wu, and S. Das Sarma, Phys. Rev. A **82**, 053611 (2010).

[56] M. Zhang, H.-H. Hung, C. Zhang, and C. Wu, Phys. Rev. A **83**, 023615 (2011).

[57] M. Milićević, T. Ozawa, G. Montambaux, I. Carusotto, E. Galopin, A. Lemaître, L. Le Gratiet, I. Sagnes, J. Bloch, and A. Amo, Phys. Rev. Lett. **118**, 107403 (2017).

[58] G. Li, W. Hanke, E. M. Hankiewicz, F. Reis, J. Schäfer, R. Claessen, C. Wu, and R. Thomale, Phys. Rev. B **98**, 165146 (2018).

[59] M. Zhou, W. Ming, Z. Liu, Z. Wang, P. Li, and F. Liu, Proc. Natl. Acad. Sci. USA **111**, 14378 (2014).

[60] T. Zhou, J. Zhang, H. Jiang, I. Žutić, and Z. Yang, npj Quantum Mater. **3**, 39 (2018).

[61] F. Reis, G. Li, L. Dudy, M. Bauernfeind, S. Glass, W. Hanke, R. Thomale, J. Schäfer, and R. Claessen, Science **357**, 287 (2017).

[62] Y. Shao, Z.-L. Liu, C. Cheng, X. Wu, H. Liu, C. Liu, J.-O. Wang, S.-Y. Zhu, Y.-Q. Wang, D.-X. Shi, K. Ibrahim, J.-T. Sun, Y.-L. Wang, and H.-J. Gao, Nano Lett. **18**, 2133 (2018).

[63] G.-F. Zhang, Y. Li, and C. Wu, Phys. Rev. B **90**, 075114 (2014).

[64] K. Nakada, M. Fujita, G. Dresselhaus, and M. S. Dresselhaus, Phys. Rev. B **54**, 17954 (1996).

[65] M. Ezawa, Phys. Rev. B **73**, 045432 (2006).

[66] Y.-W. Son, M. L. Cohen, and S. G. Louie, Phys. Rev. Lett. **97**, 216803 (2006).

[67] M. S. M. de Sousa, M. Sigrist, and W. Chen, Phys. Rev. Research **3**, 033021 (2021).

[68] Y.-W. Son, M. L. Cohen, and S. G. Louie, Nature (London) **444**, 347 (2006).

[69] F. Dominguez, B. Scharf, G. Li, J. Schäfer, R. Claessen, W. Hanke, R. Thomale, and E. M. Hankiewicz, Phys. Rev. B **98**, 161407(R) (2018).

[70] H. Rostami, R. Asgari, and F. Guinea, J. Phys.: Condens. Matter **28**, 495001 (2016).

[71] J. C. Slater and G. F. Koster, Phys. Rev. **94**, 1498 (1954).

[72] C. L. Kane and E. J. Mele, Phys. Rev. Lett. **95**, 146802 (2005).

[73] G. Manchon, S. Ghosh, C. Barreteau, and A. Manchon, Phys. Rev. B **101**, 174423 (2020).

[74] V. Bonbien and A. Manchon, Phys. Rev. B **102**, 085113 (2020).

[75] F. S. M. Guimarães, S. Lounis, A. T. Costa, and R. B. Muniz, Phys. Rev. B **92**, 220410(R) (2015).

[76] F. S. M. Guimarães, M. dos Santos Dias, J. Bouaziz, A. T. Costa, R. B. Muniz, and S. Lounis, Sci. Rep. **7**, 3686 (2017).

[77] S. Hayami, H. Kusunose, and Y. Motome, Phys. Rev. B **90**, 081115(R) (2014).

[78] C. Xiao, H. Liu, J. Zhao, S. A. Yang, and Q. Niu, Phys. Rev. B **103**, 045401 (2021).

[79] S. Hayami, M. Yatsushiro, Y. Yanagi, and H. Kusunose, Phys. Rev. B **98**, 165110 (2018).

[80] T. Furukawa, Y. Watanabe, N. Ogasawara, K. Kobayashi, and T. Itou, Phys. Rev. Research **3**, 023111 (2021).

[81] W.-Y. He and K. T. Law, Phys. Rev. Research **2**, 012073(R) (2020).

[82] A. Johansson, J. Henk, and I. Mertig, Phys. Rev. B **97**, 085417 (2018).

[83] Jülich Supercomputing Centre, J. Large-Scale Res. Facil. **4**, A132 (2018).

[84] J.-P. Hanke, F. Freimuth, A. K. Nandy, H. Zhang, S. Blügel, and Y. Mokrousov, Phys. Rev. B **94**, 121114(R) (2016).

[85] D. Go, J.-P. Hanke, P. M. Buhl, F. Freimuth, G. Bihlmayer, H.-W. Lee, Y. Mokrousov, and S. Blügel, Sci. Rep. **7**, 46742 (2017).